ACS APPLIED ENGINEERING MATERIALS

pubs.acs.org/acsaenm Article

Microstructure and Oxidation Behavior of a CrMoNbTaW Refractory High Entropy Alloy

Rebecca Romero, Irene J. Beyerlein, and C. V. Ramana*

Cite This: ACS Appl. Eng. Mater. 2023, 1, 132−139

Read Online

ACCESS | Metrics & More | Article Recommendations

ABSTRACT: This work reports on the microstructure and oxidation behavior of a refractory CrMoNbTaW high entropy alloy (HEA) produced by vacuum arc melting. Microstructure and mechanical properties of both the as-synthesized alloy and that annealed in air for 6 h in the temperature range 600−900 °C were evaluated in detail. The phase identification and microstructure analyses were performed using scanning electron microscopy (SEM), energy dispersive X-ray spectroscopy (EDX), and X-ray diffraction (XRD) while microhardness was measured using Vickers hardness tests. The as-fabricated alloy consists of a multiphase microstructure consisting of three phases: a W-rich phase, a Mo-rich phase, and a solid solution phase of BCC structure. As-synthesized HEA for this composition demonstrates excellent microhardness values, of 787 ± 83.6 HV, which was retained after annealing. The oxidation resistance in air was evaluated from 600 to 1400 °C for both 12 and 24 h of exposure time. The alloy exhibits a parabolic mass gain until 1100 °C, for which it begins to exhibit a decreasing mass gain at 1200 °C and, subsequently, a mass loss at 1300 and 1400 °C. The surface oxidation products were investigated, for which no protective oxides were identified. The surface oxide scale consisted of Cr, Nb, Ta, and trace amounts of W. The Mo content at the surface decreased as temperature increased, with no Mo content identified after 1100 °C.

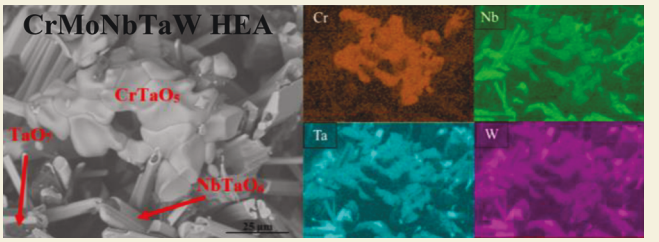

KEYWORDS: *refractory high entropy alloys, Cr−Mo−Nb−Ta−W, oxidation, microstructure*

INTRODUCTION

High entropy alloys (HEAs) have emerged as an exciting class of "applied engineering materials" with enormous potential for a wide range of structural and functional applications in energy, aerospace, power, navy, and other national security applications. The emergence of this new alloying concept of HEAs was originally presented by Yeh et. Al[1] and Cantor et. Al.[2] These early works proposed a concept that the high entropy of mixing associated with equiatomic or near-equiatomic proportions of constituent elements was enough to minimize values of Gibbs free energy.[1,2] This was typically considered for alloys consisting of five or more principal elements. The motivating factor behind these works was that the engineered alloys favored simple solid-solution microstructures rather than complex ones containing intermetallic phases. Due to the very general, composition-based definition, several studies have been conducted on HEAs since originally being proposed and have attracted much attention after demonstrating promising material properties, which can be exploited in numerous technological applications. In fact, such HEAs exhibited excellent tensile and compressive strength, ductility, microhardness, and wear resistance.[3−7] The microstructures and properties studied were mainly of transition metal HEA systems, where constituent elements included Al, Cr, Co, Cu, Fe, Ni, and Mn.[3−10] The desire to create an HEA system designed for load bearing, thermal protection applications was introduced in 2010 by Senkov et al.[11] Their study considered the use of refractory metals, which are known for their high melting temperatures, to be used as constituent elements.[11] The two systems studied were quaternary WMoNbTa and quinary WMoNbTaV alloys. Both alloys exhibited exceptional microhardness values, which far exceed those of the individual constituent elements,[11] generating significant interest in refractory-based HEAs. Such exceptional microhardness in refractory-based HEAs was attributed to a solid-solution strengthening-like mechanism.[11]

Senkov et al. established a new class of alloys, called refractory high entropy alloys (RHEAs), which are of enormous current interest. Since the novel RHEAs were introduced, many materials and/or composition tailoring of the RHEAs have been further investigated extensively.[12−17] Several of such alloys have obtained superior microhardness and compressive strengths. A CrMoNbTaV RHEA obtained an

Received: July 9, 2022
Accepted: September 16, 2022
Published: September 30, 2022

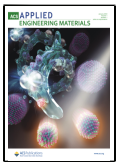

https://doi.org/10.1021/acsaenm.2c00025
ACS Appl. Eng. Mater. 2023, 1, 132−139

average microhardness value of 923 HV due to a solid solution strengthening mechanism.[14] Similarly, a $Cr_2MoNbTaVW$ RHEA obtained an average microhardness of 755 HV, both of which exhibited dendritic, BCC microstructures.[12] Due to their high melting temperatures, these refractory alloys were also subjected to studies at elevated temperatures exceeding 1200 °C. For instance, the NbMoTaW and VNbTaMoW alloys were studied up to 1600 °C.[18] At room temperature, these alloys showed limited compressive plasticity and quasicleavage fracture, which suggested that the ductile−brittle transition temperature (DBTT) was above room temperature. At higher temperatures, the alloys exhibited good plastic flow and did not show any considerable softening until a temperature of 1200 °C. The alloys were also able to retain a dendritic microstructure up to 1400 °C, which supported the concept that the high configurational entropy helped suppress constituent diffusivity.[18] The several promising results of different RHEA systems have appeared in multiple reviews.[19−21]

Although refractory metals have promise for high-temperature applications because of their high melting temperature, the main drawback of many commercial refractory alloys has been the oxidation resistance as many pure refractory metals have high rates of oxidation at elevated temperatures.[22−26] The poor oxidation resistance of the constituent elements may be related to the formation of nonprotective oxides, which can cause large volume changes and lead to spallation and cracking of oxides or forming highly volatile oxides that can be accelerated by grain boundary attack.[27] Despite having poor oxidation resistance in elemental form, some RHEAs have demonstrated adequate to good oxidation resistance, often attributed to the formation of protective oxides (e.g., Cr_2O_3, $CrTaO_4$) and slow diffusivity of oxygen.[28] In an AlSiTiCrNbMoTa RHEA, the formation of $CrTaO_4$ with a dispersion of Al_2O_3 and Cr_2O_3 helped protect the alloy, allowing it to achieve a mass gain of only 4.03 mg/cm^2 after 200 h of oxidation.[28] Increased oxidation resistance may also be related to the depressed diffusion of oxygen into the material related to one of the core concepts of sluggish diffusion of high entropy alloys.[29] Thus, several RHEAs have been studied for their oxidation resistance, as it is a vital aspect of high-temperature applications.[14,16,17,30−36] In this context, Gorr et al. recently presented a detailed review and outlined much of the research related to the oxidation behavior of these RHEAs to date.[37] Furthermore, the concept of combining different elements into HEA and the ability to tune the specific composition provides the unique ability to design high-temperature structural materials for their intended use in extreme high-temperature applications, such as turbine blades, engines, aerospace technology, and fusion reactors.[38] For instance, based on extensive work on the V−Cr−Fe−Ta−W system, Zhang et al. proposed novel low-activation $VCrFeTa_xW_x$ HEAs as a family of candidate materials for the desired applications.[38] The studies related to microstructures and mechanical properties of these HEAs with variable x clearly indicated the ability to derive tunable phase−structure−property relationships.[38] Also, as presented by Zhang in a detailed review, the entropy concept is an effective strategy for developing materials to break the property recordings of current materials, for example, breaking the trade-off between the high-strength and low-ductility structural alloys.[39] As outlined in detail as relevant to various alloys, the performance of complex alloys is derived from a balance of multiple properties, for example, combining the high strength, high ductility, high conductivity, high corrosion resistance, high irradiation resistance, etc.;[39] the strategy of HEAs is expected to provide a platform for "advanced materials design" and "development technology" to realize the goals for current and future aerospace and energy industries.[39]

The potential shown by different RHEAs has prompted the present investigation on Cr−Nb-based HEAs. Previously, we had studied the microstructure stability and oxidation (both static and cyclic) of the Cr−Nb−Ta−V−W RHEAs.[33−35] Furthermore, to investigate and comprehensively understand the chemical composition and oxide morphology evolution under oxidation, we had employed a combination of *in situ* X-ray diffraction (XRD), scanning electron microscopy (SEM), and energy dispersive X-ray spectrometry (EDX) analyses on the substrate−oxide layer interface and oxide surface.[34] These efforts had aimed to determine the early stage oxidation behavior of individual elements, including potential protective oxide formation. The combined *in situ* structural and *ex situ* microstructural and chemical analysis permitted examination and confirmation of the oxide phases and the alloy−oxide interface microstructure.[34] The microstructure near the interface indicated cracking and porosity along the interface layer which grew directionally outward. The detailed structural and chemical analyses confirmed that, while the oxide layer exhibits an increase in thickness, V was the first element to oxidize.[34] Based on all of the above points, we aimed to design a new composition of RHEA without having V in efforts to enhance microstructure stability and oxidation resistance. In this work, we present a new CrMoNbTaW alloy and engage in a detailed study into its microstructure and oxidation behavior at elevated temperatures. Here, results on the equiatomic CrMoNbTaW alloy prepared via vacuum arc melting are presented in the as-fabricated and annealed form. The oxidation behavior is also evaluated.

RESULTS AND DISCUSSION

Figure 1 presents the X-ray diffraction pattern of the as-synthesized CrMoNbTaW alloy. The pattern shows four distinct peaks at 2θ = 40.0°, 58.0°, 72.7°, and 86.4° that correspond to the diffraction from the (110), (200), (211), and (220) planes, respectively. The XRD pattern confirms the

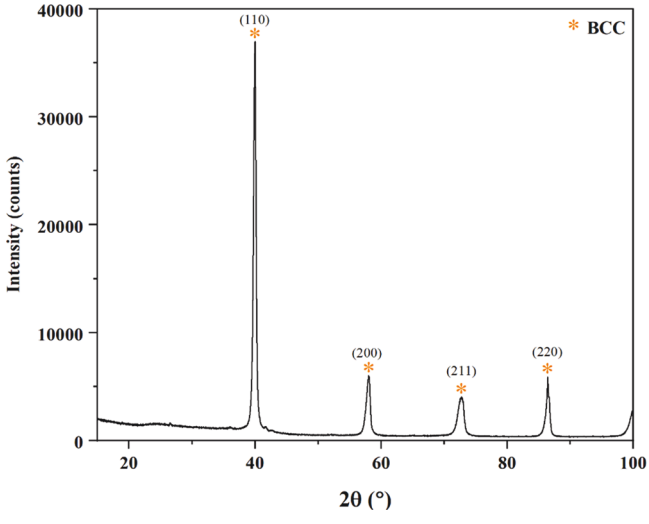

Figure 1. XRD pattern of the as-synthesized CrMoNbTaW sample.

https://doi.org/10.1021/acsaenm.2c00025
ACS Appl. Eng. Mater. 2023, 1, 132−139

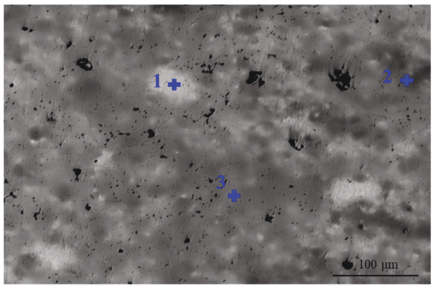

	Cr	Mo	Nb	Ta	W
Map Sum	19.7	20.3	20.3	20.4	19.3
1	16.4	10.3	15.5	14.8	43.0
2	20.2	30.2	20.2	20.2	9.2
3	23.3	18.3	20.7	19.5	18.2

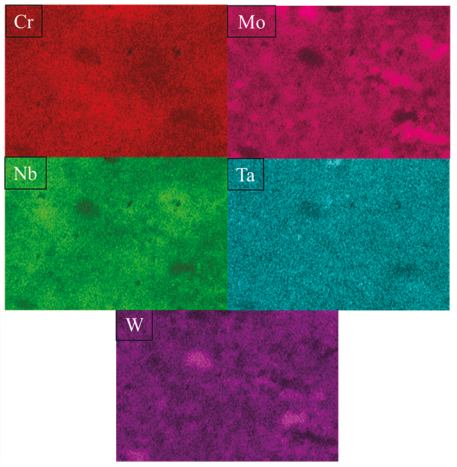

Figure 2. SEM image with corresponding EDS color mapping in BSE mode highlighting the three identified phases of the as-fabricated sample produced via vacuum arc melting.

Table 1. Tabulated Microhardness Values of the As-Synthesized HEA

location	1	2	3	4	5	6	7	8	9	10
H_v	628	805	790	851	851	665	827	769	884	843

BCC structure. Based on the pattern, the lattice constant, *a*, was determined to be 3.1951 Å.

Scanning electron microscopy (SEM) images in the backscattered electron (BSE) mode can be seen in Figure 2 with the corresponding EDS data. The surface shows some degree of porosity scattered throughout the sample. EDS analysis confirms the equiatomic nature of the five constituent elements in terms of composition of the Cr-HEA. Unlike several HEAs studied in the literature, this RHEA exhibits a multiphase microstructure consisting of three phases. The phases are identified through contrast and compositional differences. A large, white phase, identified as a W-rich (43.0 atom %) phase contains slightly depleted amounts of Cr, Nb, and Ta of similar concentrations (14.8−16.4 atom %). Mo is also present in this W-rich phase, however at slightly lower amounts, just above 10 atom %. This phase is highlighted in Figure 2. The second phase is Mo-rich (30.2 atom %), containing equiatomic amounts of Cr, Nb, and Ta (20.2 atom %). This phase is a dark, nearly black area. This phase is a counterpart to the W-rich phase, which is W-depleted in comparison to the other constituents, containing approximately 9 atom %. As the Mo−W phase diagram is isomorphous, it is reasonable that an area of enriched W would be Mo-depleted and vice versa when the area is Mo-enriched. The third phase identified is the gray region surrounding the two previously mentioned phases. This is a matrix that is nearly equiatomic of the five constituent elements and identified as area 3 (Figure 2). These three phases are highlighted by the color mapping in Figure 2.

The microhardness data is presented in Table 1. Because the differences between the W-rich and Mo-rich phase were not visible through an optical lens, the measured locations were chosen in areas free of pores on the surface. The average microhardness value is HV = 787 ± 83.6, which is higher than those of a reported quaternary alloy, MoNbTaW, which obtained an average HV = 454.3, and a quinary MoNbTaVW alloy, which obtained an average HV = 535.3. However, an alloy of similar composition,[14] but with the presence of variable Ti, is seen to present higher values than the one in this case. TiNbMoTaW alloys achieved an average HV = 950 in interdendritic regions and HV = 896 in dendritic regions.[14] The interdendritic regions were noted as having a higher Cr content than the dendritic regions, citing the increase in hardness. The presence of Cr in the present alloy as compared to the two alloys presented in ref 11 is believed to have contributed to the increased hardness. On the contrary, the addition of V increased the hardness in ref 11, so it is possible that the presence of V in ref 14, as opposed to Mo in this work, is also responsible for the superior hardness in the present alloy.

The alloy was annealed at 600, 700, 800, and 900 °C for 6 h to determine if the alloy is thermally stable and to identify if any phase changes occurred. Figure 3 presents the microstructures of the samples at their respective annealing temperature. The microstructures of the annealed samples remain consistent with the identified multiphase microstructure in the as-synthesized condition. No significant

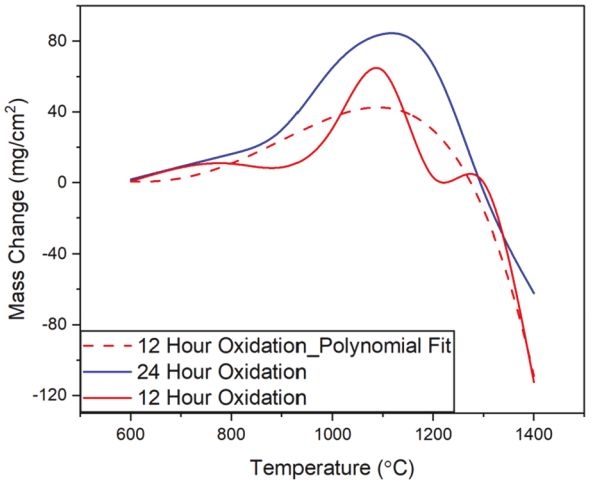

Figure 3. Oxidation curves of the mass change per surface area after 12 and 24 h of exposure for oxidation in air versus time.

https://doi.org/10.1021/acsaenm.2c00025
ACS Appl. Eng. Mater. 2023, 1, 132−139

phase changes, such as coarsening or refinement in the structure, are apparent as the temperature changes. Table 2

Table 2. Map Sum Spectrum of the Constituent Elements in Atomic Percent of Each Annealed Sample at Its Respective Temperature of Annealing

	Cr	Mo	Nb	Ta	W
600 °C	20.7	20.3	19.1	20.3	19.6
700 °C	20.8	20.2	19.3	20.3	19.4
800 °C	21.0	19.9	18.8	20.6	19.7
900 °C	21.3	19.8	18.5	20.6	19.8

presents the map sum spectra of the EDS analysis for each of the respective annealing temperatures. Each of the four temperatures shows a nearly equiatomic amount of the constituent elements at the temperatures, further indicating there is no significant change in structure. The microhardness of each annealed sample was measured. Just as the as-fabricated sample was measured, the readings were taken in the matrix areas. The results are presented in Table 3. The average

Table 3. Microhardness Results of the Annealed Samples at Their Respective Temperatures after 6 h

						mean	standard deviation
600 °C	859	851	843	790	723	812	57.2
700 °C	776	827	769	756	812	788	30.1
800 °C	867	843	867	835	820	846	20.5
900 °C	797	776	820	835	820	809	23.2

microhardness values of the annealed samples are all higher than that of the as-fabricated sample but do not show a clear trend. The standard deviation is highest in the sampled annealed at 600 °C and decreases as the annealing temperature decreases.

Samples were continuously exposed to lab air at different temperatures for both 12 and 24 h. Figure 3 presents the oxidation curve for the mass change per unit surface area of the samples. The curves shown are at 12 and 24 h at temperatures of 600, 800, 900, 1000, 1100, 1200, 1300, and 1400 °C. At both 12 and 24 h, the curves indicate a parabolic mass gain up to 1100 °C. At 1200 °C, after both 12 and 24 h of exposure, the mass change begins to decrease. At 1300 and 1400 °C, the alloys exhibit a mass loss. A curve fit is included for the 12 h oxidation curve, as a slight variation from 1200 to 1300 °C was indicated; however, because the difference is minimal, the variation is expected to be negligible.

Figure 4 shows the oxidized samples in their crucibles after exposure for both 12 and 24 h of oxidation. The samples oxidized at 600 and 800 °C show a minimal oxidation scale and a light dusting of oxide residue in the crucible. The oxide scale begins to change at 900 °C of oxidation, at which point it detaches from the remaining metal that has not been oxidized. This oxidation behavior remains up to 1100 °C. At 1200 °C, after 12 h, the oxide product is similar to that at 900−1100 °C; however, when exposed for 24 h, the oxide scale begins to grow outward in a pyramidal shape from the remaining metal. This scale is similar at 1300 °C. At 1400 °C, the oxide product is yellow and appears to remain on the metal sample.

Figures 5 and 6 present the progression of the oxide surface scale with increasing temperature. The oxide surface scale at 600 °C begins as a very rough surface texture with no definite morphology. There are a few pores present on the surface, but generally, the beginning stages of oxide growth are shown. The sample oxidized at 800 and 900 °C shows a similar surface texture but has more cracking along the surface, indicating further oxide growth. At 1000 °C, the oxide scale looks as if it has grown outward more with rounded leaflike shapes; however, the texture is still rough, like at 600 and 800 °C. At 1100 °C is when the oxide surface scale morphology begins to change, as there are small areas with some elongated areas of growth initiating after 12 h of oxidation; however, after 24 h of oxidation, it shows a more defined structure. The oxide scale at 1200 °C changes further, as the scale has a very granular texture and becomes more uniform. Significant cracking is visible throughout the surface. At 1300 °C, the surface of the oxide scale becomes more defined, and two definite morphologies of oxides can be observed: one of an elongated, rodlike structure, and one of a smaller, rounded, granular shape. The sample oxidized at 1400 °C shows a coarsened,

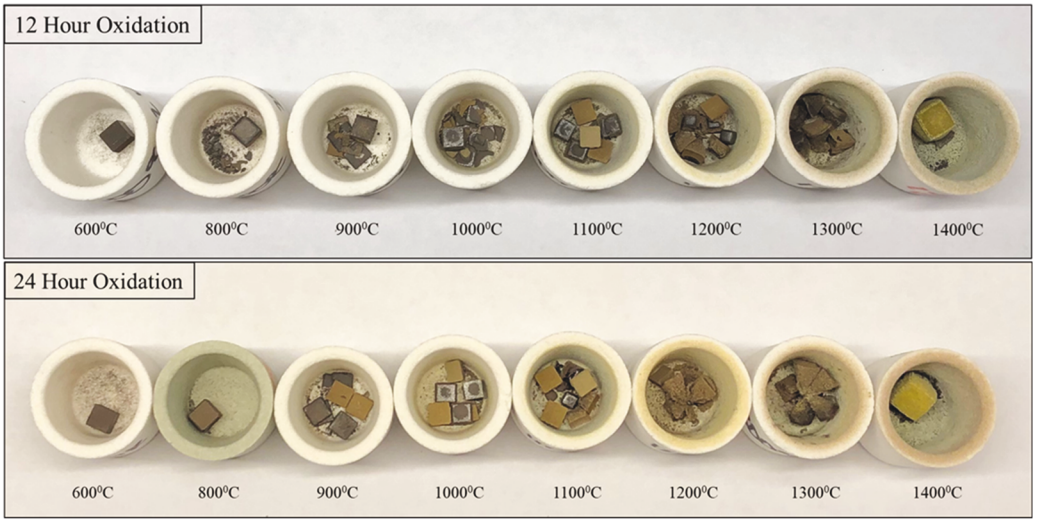

Figure 4. Physical appearance of oxidized HEA samples. The sample appearance is shown after oxidation at that respective temperature. The temperature is as indicated.

https://doi.org/10.1021/acsaenm.2c00025
ACS Appl. Eng. Mater. 2023, 1, 132−139

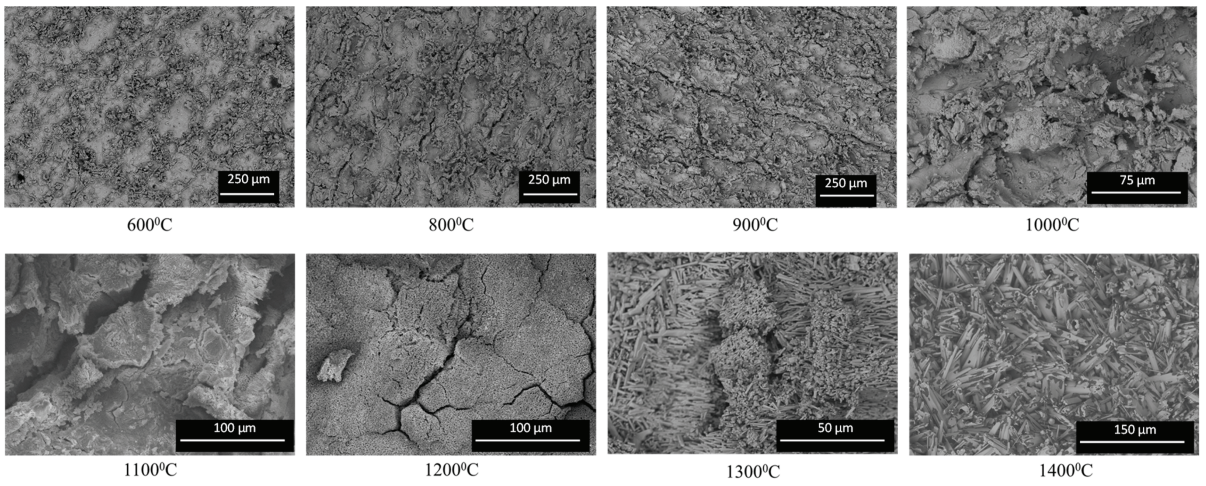

Figure 5. Surface oxide morphologies of the scale at each respective temperature after 12 h of exposure.

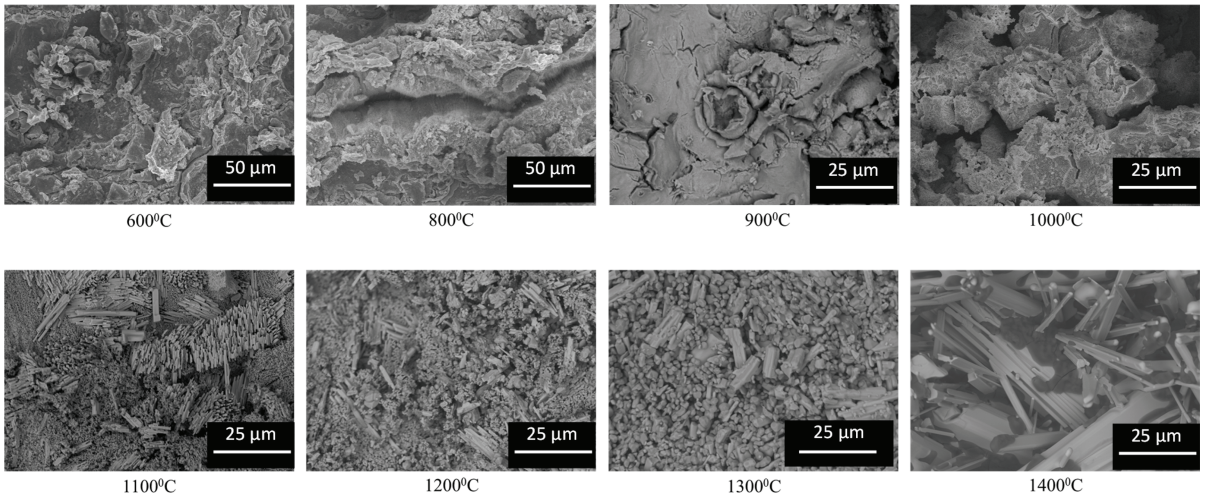

Figure 6. Surface oxide morphologies of the scale at each respective temperature after 24 h of exposure.

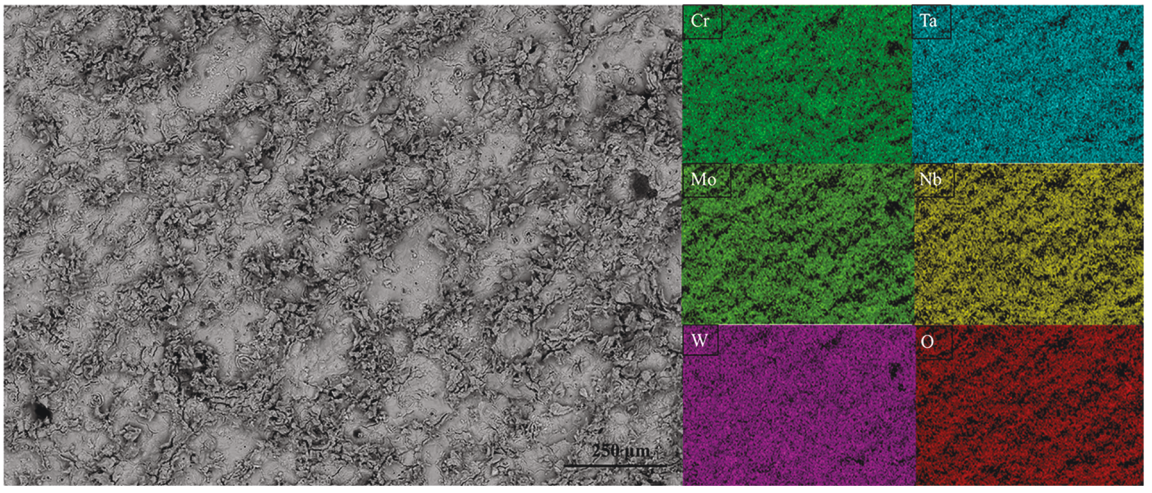

Map Sum (at. %)	
Cr	5.7
Mo	5.3
Nb	4.9
Ta	6.9
W	6.7
O	70.5

Figure 7. EDS color maps of the oxide scale after 12 h of oxidation in air at 600 °C.

rodlike structure with a darkened, black structure dispersed on the oxides.

Figure 7 displays the color map of the oxide scale for 600 °C after 12 h of oxidation. The oxide products at 24 h of exposure are similar and are not shown. The oxide scale is relatively uniform and does not indicate any segregation of any of the elements or concentrated areas. The map sum of the EDS spectrum identifies a nearly equiatomic amount of elements relative to one another. As the temperature is increased to 1100 °C (as shown in Figure 8 where the morphology begins

https://doi.org/10.1021/acsaenm.2c00025
ACS Appl. Eng. Mater. 2023, 1, 132−139

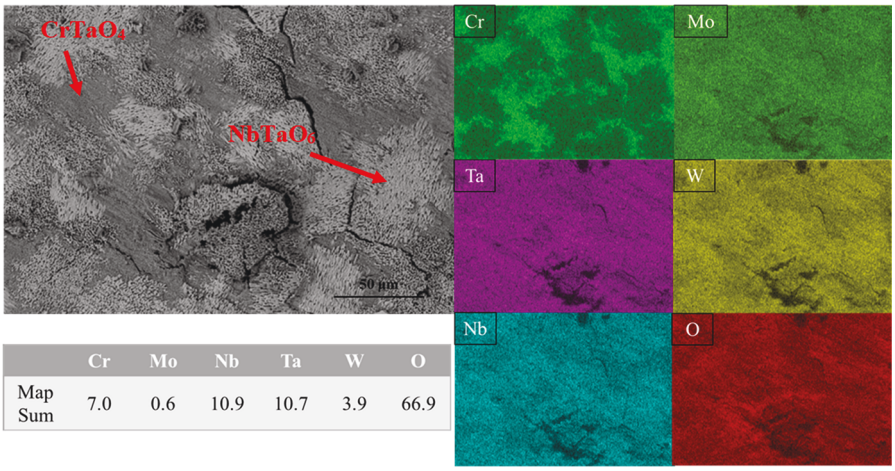

	Cr	Mo	Nb	Ta	W	O
Map Sum	7.0	0.6	10.9	10.7	3.9	66.9

Figure 8. EDS color maps of the oxide scale after 12 h of oxidation in air at 1100 °C.

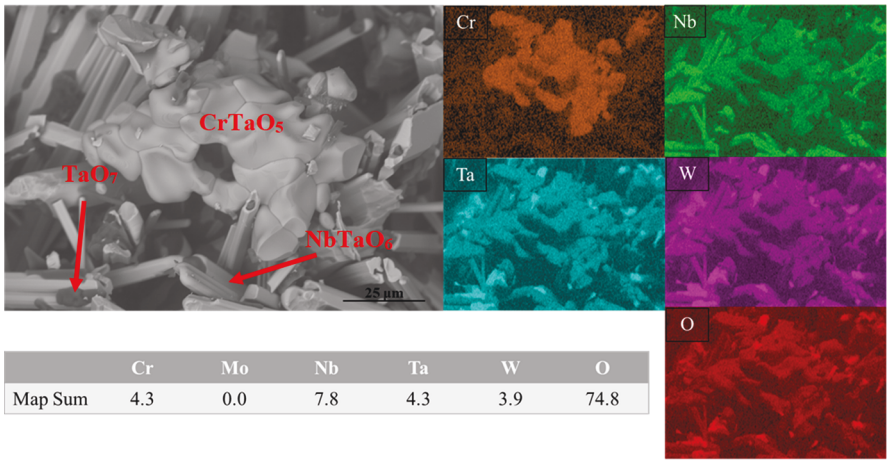

	Cr	Mo	Nb	Ta	W	O
Map Sum	4.3	0.0	7.8	4.3	3.9	74.8

Figure 9. EDS color maps of the oxide scale after 12 h of oxidation in air at 1400 °C.

to change), there is a clear indication that not only has the morphology changed, but the chemical composition of the oxides present has changed as well. There are two distinct areas, one of a Cr-rich oxide and one depleted of Cr, a uniform mixture of Mo, Nb, Ta, and W. The Cr-rich area has a chemical composition very close to $CrTaO_4$, while the mixture has a composition close to $NbTaO_6$ with trace amounts of Mo and W. The other interesting characteristic at this temperature is that the Mo content present at the surface has significantly dropped to only 0.6 atom %. At 1400 °C, well-defined oxides are now visible and evident as shown in Figure 9. There are three types of oxides present, one that is Cr-rich with a composition of $CrTaO_5$. This is the focus of the image presented, as it is a rounded, granular structure. It is surrounded by a thick, elongated structure that is Nb-rich with a composition of $NbTaO_6$. Dispersed within the two oxides is a dark, globular oxide consisting of Ta and W containing an approximate composition of TaO_7 with trace amounts of W. Mo is no longer present at the surface.

The XRD analysis was completed on samples after they were oxidized and cooled to room temperature. Figure 10 presents the XRD data of the samples at their oxidized temperature. At 600 °C, the sample still retains some BCC peaks, like those identified in the as-fabricated condition. There are also some peaks indicating a Ta_2WO_8 structure and $CrTaO_4$ or $CrNbO_4$ structure. At 800 °C, the peaks related to the BCC structure

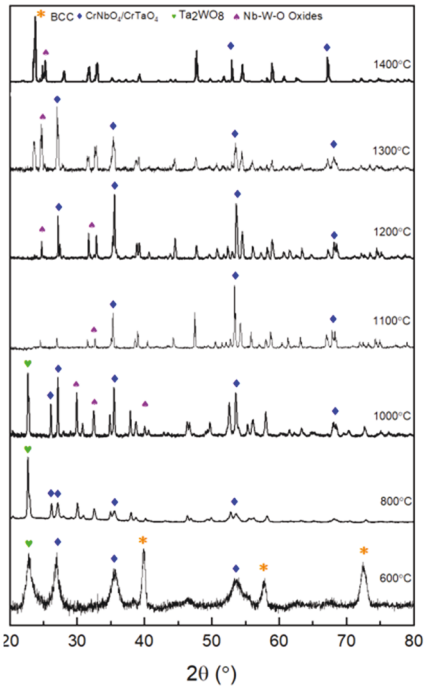

Figure 10. XRD of the oxidized samples after 12 h of oxidation in air.

https://doi.org/10.1021/acsaenm.2c00025
ACS Appl. Eng. Mater. 2023, 1, 132−139

are no longer visible, indicating the surface has oxidized. The oxides seen are like those at 600 °C. As the temperature increases, the peaks become stronger.

CONCLUSIONS

The structure and microstructure of as-synthesized refractory CrMoNbTaW alloy was evaluated. The microstructure revealed a multiphase microstructure, which consists of one W-rich phase with a bright, white appearance and a Mo-rich phase, which has a dark, rounded, black appearance. The two phases are surrounded by a gray matrix of a nearly equiatomic solution of the five constituent elements. The XRD results revealed that the refractory CrMoNbTaW alloy retained the BCC structure. The refractory CrMoNbTaW alloy exhibited excellent microhardness values, which are either comparable or exceeding values reported for other RHEAs. No significant changes in the crystal structure or microstructure were present when the refractory CrMoNbTaW alloy was annealed in the temperature range 600−900 °C for 6 h. Further, the microhardness values of the annealed CrMoNbTaW samples did not differ significantly from the as-fabricated samples, indicating thermal stability and showing no significant softening after exposure to elevated temperatures. Oxidation of the alloy at 12 and 24 h in the temperature range from 600 to 1400 °C initially showed a parabolic mass gain until 1200 °C, where the mass gain began to decrease and at 1300 and 1400 °C experienced mass loss. The alloy was considered to have adequate oxidation resistance up to 1000 °C. The surface oxidation layers revealed similar structures after both 12 and 24 h of oxidation at respective temperatures. At 800 °C the oxide surface began to show a decrease in Mo content on the surface, until which there was little to no Mo seen at the surface beginning around 1100 °C. As oxidation temperature increased, the oxide morphology became more defined. There were two distinct oxides in the temperature range from 1100 to 1300 °C of an elongated Ta−W−Nb oxide and a granular Cr oxide. At 1400 °C at both oxidation times, the oxides change to an elongated Nb-rich oxide with dispersed black, globular oxides of Ta and W.

EXPERIMENTAL DETAILS

The cubes of Cr−Mo−Nb−Ta−W HEAs were procured from Plasma Materials Inc. (Livermore, CA) and were fabricated by arc melting using metals of at least three nines purity. The as-received cubes were cut by electrical discharge machining (EDM). Specimens were annealed and oxidized from the as-received state in a muffle box air furnace placed in an alumina crucible, at respective times and temperatures. Annealed samples were subjected to a 6 h anneal at temperatures from 600 to 900 °C. Oxidized samples were subjected to oxidation temperatures of 600 and 800−1400 °C for both 12 and 24 h. A heating rate of 10 °C/min was utilized up to the selected annealed or oxidation temperature. The samples were then cooled to room temperature inside the furnace.

To observe the microstructures and oxidized surface layers, scanning electron microscopy (SEM, Hitachi High-Tech America, Inc.) was performed using the backscattered electron mode. The EDS system did not use standards. The EDS analyses is known to help to identify various elements present in the simple metals, alloys, and complex oxides in addition to information on the chemical homogeneity[40,41]. The compositions of the phases and oxide products were determined by EDS with the use of X-ray color mapping to allow for the determination of elements.

The phases and structure of the alloys were identified by X-ray diffraction (XRD, D8 Discover with Cu Kα radiation, Karlsruhe, Germany). XRD analysis was performed on an unmounted sample. Prior to the examination, the sample was cleaned in an ultrasonic cleaner for 2 min in ethanol.

AUTHOR INFORMATION

Corresponding Author

C. V. Ramana − *Center for Advanced Materials Research, University of Texas at El Paso, El Paso, Texas 79968, United States; Department of Mechanical Engineering, University of Texas, El Paso, Texas 79968, United States;* orcid.org/0000-0002-5286-3065; Email: rvchintalapalle@utep.edu

Authors

Rebecca Romero − *Center for Advanced Materials Research, University of Texas at El Paso, El Paso, Texas 79968, United States; Department of Metallurgical, Materials and Biomedical Engineering, University of Texas, El Paso, Texas 79968, United States*

Irene J. Beyerlein − *Department of Mechanical Engineering, University of California, Santa Barbara, California 93106-5070, United States; Materials Department, University of California, Santa Barbara, California 93016-5050, United States*

Complete contact information is available at: https://pubs.acs.org/10.1021/acsaenm.2c00025

Notes

The authors declare no competing financial interest.

ACKNOWLEDGMENTS

This work is a contribution from the Center for Advanced Materials Research (CMR). The authors at the University of Texas at El Paso acknowledge, with pleasure, support from the National Science Foundation with NSF-PREM grant DMR-1827745. I.J.B. gratefully acknowledges support from the Office of Naval Research under contract N00014-21-1-2536

REFERENCES

(1) Yeh, J. W.; Chen, S. K.; Lin, S. J.; Gan, J. Y.; Chin, T. S.; Shun, T. T.; Tsau, C. H.; Chang, S. Y. Nanostructured high-entropy alloys with multiple principal elements: Novel alloy design concepts and outcomes. *Adv. Eng. Mater.* **2004**, *6*, 299−303.

(2) Cantor, B.; Chang, I. T. H.; Knight, P.; Vincent, A. J. B. Microstructural development in equiatomic multicomponent alloys. *Mater. Sci. Eng., A* **2004**, *375*−*377*, 213−218.

(3) Zhang, K. B.; Fu, Z. Y.; Zhang, J. Y.; Wang, W. M.; Wang, H.; Wang, Y. C.; Zhang, Q. J.; Shi, J. Microstructure and mechanical properties of CoCrFeNiTiAlx high-entropy alloys. *Mater. Sci. Eng., A* **2009**, *508*, 214−219.

(4) Shun, T. T.; Du, Y. C. Microstructure and tensile behaviors of FCC Al0.3CoCrFeNi high entropy alloy. *J. Alloys Compd.* **2009**, *479*, 157−160.

(5) Tong, C. J.; Chen, Y. L.; Chen, S. K.; Yeh, J. W.; Shun, T. T.; Tsau, C. H.; Lin, S. J.; Chang, S. Y. Microstructure characterization of AlxCoCrCuFeNi high-entropy alloy system with multiprincipal elements. *Metall. Mater. Trans. A Phys. Metall. Mater. Sci.* **2005**, *36*, 881−893.

(6) Tong, C. J.; Chen, M. R.; Chen, S. K.; Yeh, J. W.; Shun, T. T.; Lin, S. J.; Chang, S. Y. Mechanical performance of the AlxCoCrCuFeNi high-entropy alloy system with multiprincipal elements. *Metall. Mater. Trans. A Phys. Metall. Mater. Sci.* **2005**, *36*, 1263−1271.

(7) Wang, Y. P.; Li, B. S.; Ren, M. X.; Yang, C.; Fu, H. Z. Microstructure and compressive properties of AlCrFeCoNi high entropy alloy. *Mater. Sci. Eng., A* **2008**, *491*, 154−158.

(8) Hsu, C. Y.; Wang, W. R.; Tang, W. Y.; Chen, S. K.; Yeh, J. W. Microstructure and mechanical properties of new AlCoxCrFeMo 0.5Ni high-entropy alloys. *Adv. Eng. Mater.* **2010**, *12*, 44−49.
(9) Wang, F.; Zhang, Y.; Chen, G.; Davies, H. A. Tensile and compressive mechanical behavior of a CoCrCuFeNiAl0.5 high entropy alloy. *Int. J. Mod. Phys. B* **2009**, *23*, 1254−1259.
(10) Hsieh, K. C.; Yu, C. F.; Hsieh, W. T.; Chiang, W. R.; Ku, J. S.; Lai, J. H.; Tu, C. P.; Yang, C. C. The microstructure and phase equilibrium of new high performance high-entropy alloys. *J. Alloys Compd.* **2009**, *483*, 209−212.
(11) Senkov, O. N.; Wilks, G. B.; Miracle, D. B.; Chuang, C. P.; Liaw, P. K. Refractory high-entropy alloys. *Intermetallics* **2010**, *18*, 1758−1765.
(12) Zhang, B.; Gao, M. C.; Zhang, Y.; Guo, S. M. Senary refractory high-entropy alloy CrxMoNbTaVW. *Calphad Comput. Coupling Phase Diagrams Thermochem.* **2015**, *51*, 193−201.
(13) Yao, H. W.; Qiao, J. W.; Gao, M. C.; Hawk, J. A.; Ma, S. G.; Zhou, H. F.; Zhang, Y. NbTaV-(Ti,W) refractory high-entropy alloys: Experiments and modeling. *Mater. Sci. Eng., A* **2016**, *674*, 203−211.
(14) Han, Z. D.; Luan, H. W.; Liu, X.; Chen, N.; Li, X. Y.; Shao, Y.; Yao, K. F. Microstructures and mechanical properties of TixNbMo-TaW refractory high-entropy alloys. *Mater. Sci. Eng., A* **2018**, *712*, 380−385.
(15) Xiao, Y.; Kuang, W.; Xu, Y.; Wu, L.; Gong, W.; Qian, J.; Zhang, Q.; He, Y. Microstructure and oxidation behavior of the CrMoNbTaV high-entropy alloy. *J. Mater. Res.* **2019**, *34*, 301−308.
(16) Senkov, O. N.; Woodward, C. F. Microstructure and properties of a refractory NbCrMo0.5Ta0.5TiZr alloy. *Mater. Sci. Eng., A* **2011**, *529*, 311−320.
(17) Liu, C. M.; Wang, H. M.; Zhang, S. Q.; Tang, H. B.; Zhang, A. L. Microstructure and oxidation behavior of new refractory high entropy alloys. *J. Alloys Compd.* **2014**, *583*, 162−169.
(18) Gorr, B.; Mueller, F.; Christ, H. J.; Mueller, T.; Chen, H.; Kauffmann, A.; Heilmaier, M. High temperature oxidation behavior of an equimolar refractory metal-based alloy with and without Si addition. *J. Alloys Compd.* **2016**, *688*, 468−477.
(19) Senkov, O. N.; Wilks, G. B.; Scott, J. M.; Miracle, D. B. Mechanical properties of Nb25Mo25Ta 25W25 and V20Nb20Mo 20Ta20W20 refractory high entropy alloys. *Intermetallics* **2011**, *19*, 698−706.
(20) Chen, J.; Zhou, X.; Wang, W.; Liu, B.; Lv, Y.; Yang, W.; Xu, D.; Liu, Y. A review on fundamental of high entropy alloys with promising high-temperature properties. *J. Alloys Compd.* **2018**, *760*, 15−30.
(21) Couzinié, J. P.; Senkov, O. N.; Miracle, D. B.; Dirras, G. Comprehensive data compilation on the mechanical properties of refractory high-entropy alloys. *Data Br.* **2018**, *21*, 1622−1641.
(22) Senkov, O. N.; Miracle, D. B.; Chaput, K. J.; Couzinie, J. P. Development and exploration of refractory high entropy alloys - A review. *J. Mater. Res.* **2018**, *33*, 3092−3128.
(23) Gulbransen, E. A.; Andrew, K. F. Kinetics of the Oxidation of Chromium. *J. Electrochem. Soc.* **1957**, *104*, 334.
(24) Mukherjee, A.; Wach, S. P. Kinetics of the oxidation of vanadium in the temperature range 350−950°C. *J. Less-Common Met.* **1983**, *92*, 289−300.
(25) Price, W. R.; Stringer, J. Stringer The oxidation of vanadium at high temperatures. *J. of the Less Common Metals* **1965**, *8*, 165−185.
(26) Kubaschevaki, O.; Hopkins, B. E. Oxidation of Metals and Alloys, Acadlc Press: N. Y. 1962.
(27) Perkins, R. A.; Meier, G. H. The oxidation behavior and protection of niobium. *JOM* **1990**, *42*, 17−21.
(28) Butler, T. M. High Entropy Alloys: Oxidation. *Encycl. Mater. Met. Alloy.* **2021**, *2*, 522−532.
(29) Lo, K. C.; Chang, Y. J.; Murakami, H.; Yeh, J. W.; Yeh, A. C. An oxidation resistant refractory high entropy alloy protected by CrTaO 4 -based oxide. *Sci. Rep.* **2019**, *9*, 3−4.
(30) Miracle, D. B.; Senkov, O. N. A critical review of high entropy alloys and related concepts. *Acta Mater.* **2017**, *122*, 448−511.
(31) Gorr, B.; Müller, F.; Azim, M.; Christ, H. J.; Müller, T.; Chen, H.; Kauffmann, A.; Heilmaier, M. High-Temperature Oxidation Behavior of Refractory High-Entropy Alloys: Effect of Alloy Composition. *Oxid. Met.* **2017**, *88*, 339−349.
(32) Gorr, B.; Azim, M.; Christ, H. J.; Mueller, T.; Schliephake, D.; Heilmaier, M. Phase equilibria, microstructure, and high temperature oxidation resistance of novel refractory high-entropy alloys. *J. Alloys Compd.* **2015**, *624*, 270−278.
(33) Varma, S. K.; Sanchez, F.; Moncayo, S.; Ramana, C. V. Static and cyclic oxidation of Nb-Cr-V-W-Ta high entropy alloy in air from 600 to 1400 °C. *J. Mater. Sci. Technol.* **2020**, *38*, 189−196.
(34) Romero, R. R.; Makeswaran, N. M.; Naraparaju, R.; Ramana, C. V. Examination of the oxidation and metal-oxide layer interface of a Cr-Nb-Ta-V-W high entropy alloy at elevated temperatures. *Adv. Eng. Mater.* **2021**, *23*, 2100164.
(35) Varma, S. K.; Sanchez, E. F.; Ramana, C. V. Microstructures in a Nb-Cr-V-W-Ta high entropy alloy during annealing. *J. Mater. Sci. Technol.* **2020**, *53*, 66−72.
(36) Osei-Agyemang, E.; Balasubramanian, G. Surface oxidation mechanism of a refractory high-entropy alloy. *npj Mater. Degrad.* **2019**, *3*, 1.
(37) Gorr, B.; Schellert, S.; Müller, F.; Christ, H. J.; Kauffmann, A.; Heilmaier, M. Current Status of Research on the Oxidation Behavior of Refractory High Entropy Alloys. *Adv. Eng. Mater.* **2021**, *23*, 2001047.
(38) Zhang, W.; Liaw, P. K.; Zhang, Y. A Novel Low-Activation $VCrFeTa_xW_x$ (x = 0.1, 0.2, 0.3, 0.4, and 1) High-Entropy Alloys with Excellent Heat-Softening Resistance. *Entropy* **2018**, *20*, 951.
(39) Zhang, Y.; Yan, X. Breaking the Property Trade-Offs by Using Entropic Conceptions. In *High Entropy Materials - Microstructures and Properties*; Zhang, Y. A., Ed.; Intechopen Press, 2022.
(40) Ramana, C.V.; Ait-Salah, A.; Utsunomiya, S.; Morhange, J.F.; Mauger, A.; Gendron, F.; Julien, C.M. Spectroscopic and Chemical Imaging Analysis of Lithium Iron Triphosphate. *J. Phys. Chem. C* **2007**, *111*, 1049−1054.
(41) Ramana, C.V.; Ait-Salah, A.; Utsunomiya, S.; Mauger, A.; Gendron, F.; Julien, C.M. Novel Lithium Iron Pyrophosphate (LiFe1.5P2O7) as a Positive Electrode for Li-Ion Batteries. *Chem. Mater* **2007**, *19*, 5319−5324.

https://doi.org/10.1021/acsaenm.2c00025
ACS Appl. Eng. Mater. 2023, 1, 132−139